Materials Advances

ROYAL SOCIETY OF CHEMISTRY

PAPER

View Article Online
View Journal

Check for updates

Cite this: DOI: 10.1039/d6ma00556j

Green biosynthesis of silver nanoflowers using the *Tithonia diversifolia* leaf extract: *in vitro* anticancer activity, antimetastatic effects, and crystal violet photodegradation

Suganya Ganesan,[ac] Aswathy Karanath-Anilkumar,[bc] Jerome Rajendran *[d] and Ganesh Munuswamy-Ramanujam *[ac]

Received 21st April 2026,
Accepted 27th May 2026

DOI: 10.1039/d6ma00556j

rsc.li/materials-advances

The convergence of cancer incidence, persistent infectious wounds, and environmental contamination by industrial dyes such as crystal violet underscores the need for sustainable nanomaterials that can support both biomedical and environmental applications. In this study, silver nanoflowers (AgNFs) were synthesized through a green aqueous route using the *Tithonia diversifolia* leaf extract (TDLE) as a reducing and stabilizing medium. This plant-mediated strategy was selected to minimize chemical input while exploiting the phytochemical constituents of TDLE for silver-ion reduction, surface capping, and hierarchical nanostructure formation. Ultraviolet-visible (UV-vis) spectroscopy showed a characteristic silver plasmonic absorption band, while Fourier transform infrared (FT-IR) spectroscopy supported the involvement of extract-derived hydroxyl, carbonyl, and carboxyl-containing functional groups in surface capping. X-ray diffraction (XRD) confirmed crystalline face-centered cubic silver with preferential reflection features, and scanning electron microscopy (SEM) and transmission electron microscopy (TEM) revealed radially assembled flower-like architectures composed of petal-like silver plates. Selected area electron diffraction (SAED) further supported the polycrystalline nature of the NFs, while zeta-potential analysis and dynamic light scattering (DLS) analysis indicated aqueous dispersion behaviour consistent with phytochemical-assisted electrosteric stabilization. Thermogravimetric analysis (TGA) confirmed the presence of surface-associated organic capping components, and Brunauer–Emmett–Teller (BET) analysis showed mesoporous textural features with a surface area of 36.7 $m^2\ g^{-1}$, supporting accessible interfacial surface sites. Functionally, the TDLE-derived AgNFs (TD-AgNFs) showed concentration-dependent anticancer activity, with IC_{50} values of 160, 230, and 260 $\mu g\ mL^{-1}$ against Huh7, THP-1, and SiHa cancer cell models, respectively. TD-AgNFs also reduced *in vitro* cancer cell migration under scratch and transwell assay conditions at 50 $\mu g\ mL^{-1}$. In addition, TD-AgNFs enabled rapid sunlight-assisted crystal violet photodegradation across 5–25 ppm, as estimated from UV-vis absorbance changes. Overall, the findings support TD-AgNFs as plant-derived hierarchical silver nanostructures with preliminary *in vitro* biomedical activity and sunlight-assisted dye-degradation performance, while further mechanistic, selectivity, and mineralization studies are required for deeper validation.

1. Introduction

Advancing therapeutic and environmental health solutions that simultaneously address cancer, wound healing, and water pollution is an urgent interdisciplinary challenge in 2025 because all three place growing pressure on public health and the environment, and the urgency is clear in both the scale of the burden and its upward trajectory.[1] Cancer incidence reached about 20 million new cases and 9.7 million deaths in 2022 and is projected to rise to about 35 million new cases by 2050, signalling a sustained need for therapies that act where

---

[a] *Department of Chemistry, College of Science and Humanities, SRM Institute of Science & Technology, Kattankulathur, Chengalpattu 603203, India. E-mail: mrganesh2000@hotmail.com, ganeshm1@srmist.edu.in*
[b] *Department of Biotechnology, College of Engineering and Technology, SRM Institute of Science & Technology, Kattankulathur, Chengalpattu 603203, India*
[c] *Interdisciplinary Institute of Indian System of Medicine, SRM Institute of Science & Technology, Kattankulathur, Chengalpattu 603203, India*
[d] *Department of Electrical Engineering and Computer Science, University of California Irvine, CA, USA. E-mail: jeromestil@gmail.com, rajendrj@uci.edu*

tumour cells survive and metastasize.[2] Industrial dye effluents worsen the problem of water quality because textile dyeing and finishing contribute roughly 17%–20% of industrial water pollution, with an estimated 280 000 tonnes of dyes entering the environment each year.[3] Crystal violet, a widely used cationic dye, is listed as a suspected carcinogen and is very toxic to aquatic life, so its removal is both a regulatory and public health priority.[4] These domains connect mechanistically because short-lived reactive species control outcomes at soft and liquid interfaces, with reactive oxygen supporting or derailing wound closure, sustaining cancer programmes when unchecked, and driving dye breakdown when channelled into radical pathways.[5] This convergence motivates the development of materials that can modulate interfacial reactive chemistry in cells and in water while being produced by routes that minimise added risk to people and ecosystems.

In recent years, silver nanoparticles (AgNPs) have attracted considerable attention due to their distinctive physicochemical properties compared to bulk materials and their broad technological potential across multiple sectors.[6] Among these, flower-shaped hierarchical three-dimensional nanostructures, commonly termed ''nanoflowers (NFs),'' are especially compelling because their high surface-to-volume ratios enhance interfacial reactivity, and they can often be produced at low costs using eco-friendly methods.[7] Nanomedicine, defined as the convergence of nanoscience and nanotechnology for medical applications, is transforming disease diagnosis, therapy, and prevention, with particular promise in gene and cancer therapies.[8] Conventional medical approaches, however, frequently suffer from low efficacy, adverse side effects, toxicity, slow/poor clearance, and limited tissue or cellular targeting.[9,10] Consequently, engineered nanomaterials have emerged as multifaceted platforms for targeted drug and gene delivery. At the same time, concerns surrounding the biocompatibility, biosafety, and environmental footprint of NPs produced *via* traditional physicochemical routes have accelerated the shift toward green and biogenic synthetic strategies that leverage biological extracts to reduce toxicity and improve safety.[11] Within this context, NFs, which are complex flower-like architectures of metals or metal oxides, stand out for their large accessible surface areas, unique physical properties, and enhanced bioactivity, which enable a wide range of biomedical applications.[12] More broadly, rapid advances in nanotechnology are reshaping fields such as agriculture, energy, catalysis, and environmental remediation, driven by quantum-scale effects and high surface area-to-volume ratios. Metal and metal-oxide systems, including silver (Ag),[13] gold (Au), and zinc oxide (ZnO),[14] as well as complex bi- and trimetallic NFs, have demonstrated robust antibacterial and antifungal activities,[15] along with anticancer and diagnostic capabilities.

Escalating antibiotic resistance further underscores the need for new antimicrobial strategies. Nanomaterials can compromise bacterial viability through cell wall disruption, oxidative stress, and protein or DNA inactivation—mechanisms that are comparatively less prone to resistance. A pivotal development supporting safer translation is green synthesis, which uses plant extracts, fungi, algae, yeasts, or bacterial biomass as reducing and capping agents to yield biocompatible nanomaterials with a reduced environmental burden.[16] In particular, plant-mediated routes exploit phytochemicals such as polyphenols, flavonoids, and alkaloids to produce stable NPs and NFs that resist aggregation and exhibit potent biological activity. This sustainable approach also enables fine control over the morphology and bioactivity, as shown by diverse ZnO and AgNFs with superior antimicrobial, antifungal, and anticancer performance.[17]

Emerging evidence further highlights the potential of biogenic nanostructures, from mycosynthesized AgNPs with antibacterial, anticancer, and scratch-assay activity[18] to rosemary-phenolic-assisted NiCoFe$_2$O$_4$ nanoflowers that function as magnetically assisted non-viral gene-delivery nanocarriers with low *in vitro* cytotoxicity under the tested conditions.[19] Despite these advances, a central challenge remains: the design of safe, efficient, and multifunctional nanocarriers that are suitable for clinical translation, particularly in gene therapy, where immune responses and off-target effects must be tightly controlled.[19] The current research, therefore, focuses not only on clarifying how the size, shape, and surface chemistry govern biological interactions and efficacy, but also on refining scalable, reproducible, and environmentally benign synthetic routes.[20] By integrating green nanotechnology, plant phytochemistry, and nanostructure engineering, the field is poised to deliver innovative, biocompatible nanomaterials for next-generation biomedical and antimicrobial applications.[21]

Here, we selected *Tithonia diversifolia* (Mexican sunflower) because it is widely available, is traditionally used to treat gastrointestinal disorders, and has been reported to contain phenolic acids, flavonoids, tannins, sesquiterpene lactones, and other antioxidant-associated phytochemicals that contribute to its biological activity.[22–26] Based on the reported phytochemical composition of *T. diversifolia* and the FT-IR evidence obtained in this study, hydroxyl, carboxyl, and carbonyl-containing biomolecules in the extract may participate in Ag$^+$ reduction and surface capping during AgNFs formation.[27] The resulting high-surface-area architectures and plasmonic properties, together with a phytochemical corona, may enhance antibacterial performance by improving cell-envelope contact, surface-mediated redox interactions, and Ag-based antimicrobial activity.[28] In anticancer applications, bioactive constituents such as sesquiterpene lactones and Ag-mediated interfacial redox effects may contribute to reduced cancer cell viability, while surface capping can improve colloidal stability and support reproducible interaction with representative tumour cell lines.[29] For photocatalytic dye removal, facet-rich NFs provide abundant surface sites that, together with residual phytochemicals aiding dispersion, may promote light-assisted interaction with model dyes in water under benign conditions.[30] Collectively, these attributes justify the *T. diversifolia* leaf extract (TDLE) as a green, scalable biogenic platform for synthesizing TD-AgNFs tailored to antibacterial, anticancer, and photocatalytic reduction applications.

Although plant-mediated synthesis of Ag-based nanomaterials has been extensively reported, the majority of available studies remain focused on conventional spherical or irregular AgNPs, mixed Ag-based phases, or isolated demonstrations of antibacterial, anticancer, antioxidant, or photocatalytic activity. Therefore, the novelty of the present work is not only the green antimigratory reduction of Ag^+ ions, but also the use of *T. diversifolia* phytochemistry to direct the formation of hierarchical metallic AgNFs with petal-like architectures, phytochemical surface functionality, and mesoporous textural features. This distinction is important because the flower-like morphology provides a high density of exposed edges and accessible interpetal spaces, while the plant-derived surface corona contributes to reduction, capping, and colloidal stabilization. Compared with recent plant-mediated AgNPs and AgNFs summarized in Table S1, the presented TD-AgNFs system integrates structural hierarchy, BET-supported mesoporosity, anticancer activity, *in vitro* cancer cell migration inhibition, antimicrobial/antifungal activity, antioxidant/ROS response, and sunlight-assisted crystal violet degradation within a single green-synthesized platform. This structure–function integration establishes the central novelty of the study and differentiates the presented TD-AgNFs from previously reported green-synthesized Ag systems that primarily report particle formation with selected biological or photocatalytic endpoints.

To realize these aims, TD-AgNFs were synthesized through a purely aqueous green route using TDLE as both a reductant and a stabilizer, leveraging its distinctive phytochemical matrix to direct hierarchical growth. Comprehensive characterization supported the formation of well-defined flower-like architectures: UV-vis spectroscopy showed a surface plasmon band consistent with anisotropic silver domains; FT-IR spectroscopy indicated the coordination of plant-derived functional groups on the Ag surface; powder X-ray diffraction confirmed face-centered cubic silver with a pronounced (111) reflection; and high-resolution SEM and TEM resolved uniform petal-like plates assembled into multilayered flowers. The SAED pattern exhibited clear concentric rings, indicating the polycrystalline nature of the NFs. Colloidal stability in physiologically relevant media was verified by ζ-potential measurements, thermogravimetric analysis indicated robust thermal tolerance, and BET porosimetry measured a mesoporous surface area of 36.7 $m^2\ g^{-1}$. Functionally, TD-AgNFs showed anticancer activity, with IC_{50} values of 160, 230, and 260 $\mu g\ mL^{-1}$ in Huh7, THP-1, and SiHa models, respectively; exhibited *in vitro* antimigratory activity under scratch and transwell assay conditions at 50 $\mu g\ mL^{-1}$; and enabled sunlight-driven photodegradation of crystal violet across 5–25 ppm, thereby establishing a sustainable route to structurally well-defined, stable, high-surface-area TD-AgNFs and motivating the subsequent antibacterial, anticancer, antimigratory, and photocatalytic investigations.

2. Results and discussion

2.1. Synthesis and physicochemical characterization of TD-AgNFs

Addressing persistent bacterial infection, tumour cytotoxicity at tolerable doses, and sunlight-driven dye remediation requires a material that combines strong interfacial redox chemistry, efficient light harvesting, and stability in aqueous media. Silver satisfies these functional requirements through complementary mechanisms.[31] At the cell or microbe interface, metallic Ag and possible Ag^+ release have been associated with membrane interactions, enzyme disruption, and redox imbalance, which may contribute to the observed antimicrobial and anticancer responses (Fig. 1). Under illumination, the localized surface plasmon response of Ag may facilitate interfacial light–matter interactions and charge-transfer processes, supporting dye degradation in water without added harsh reagents.[21] To realize these outcomes through a sustainable route, *T. diversifolia* was selected as the biogenic source because previous reports describe its leaves as rich in polyphenols, flavonoids, phenolic acids, and sesquiterpene lactones, while the FT-IR results in this study indicate the presence of hydroxyl, carbonyl, and carboxyl-containing groups that may participate in Ag^+ reduction and surface coordination.[32] During synthesis, phytochemical constituents containing hydroxyl, carbonyl, and carboxyl groups likely participate in Ag^+ reduction and surface coordination, while differential adsorption on growing Ag domains may assist anisotropic growth and flower-like assembly formation. According to FT-IR and TGA observations, the residual organic surface layer may contribute to dispersion behaviour and surface accessibility during biological and photocatalytic assays.[33] The material was produced by plant-mediated aqueous colloidal reduction using $AgNO_3$ as a precursor and the leaf extract as the sole reductant and capping agent under ambient conditions (as shown in Fig. 1 and Fig. S1A, B), followed by purification and gentle drying to isolate stable AgNFs whose structure and performance are examined in the following sections.

After synthesis, the black TD-AgNFs solid was redispersed in water to obtain a stable colloidal dispersion used for all subsequent assays. UV-Vis spectroscopy was chosen as the first probe because it directly reports the localized surface plasmon resonance of metallic silver and therefore verifies the $Ag^+ \rightarrow Ag^0$ reduction,[34] gives a preliminary understanding of the particle morphology and aggregation state, and flags the presence of nonmetallic byproducts. The dispersion exhibits a broad extinction band with a maximum centred in the blue region at ∼390 nm, within the highlighted 350–450 nm window, accompanied by a gentle shoulder in the near-UV region (≈270–300 nm) and a long, gradually decaying tail toward the visible-NIR region (Fig. 2A). The principal band confirms the formation of metallic Ag domains; its breadth and modest redward tail are consistent with anisotropic, petal-rich architectures, in which facet coupling and thickness dispersion broaden the ensemble resonance relative to small spherical Ag colloids. The near-UV shoulder arises from residual aromatic phytochemicals and the interband contributions of Ag, indicating that a thin organic corona remains on the surface, which is desirable for colloidal stability. No discrete features attributable to silver salts or oxide impurities are evident within the 450–800 nm region, and the smooth baseline indicates minimal large-scale agglomeration. Taken together, the spectrum verifies the complete reduction to Ag^0, supports the presence of

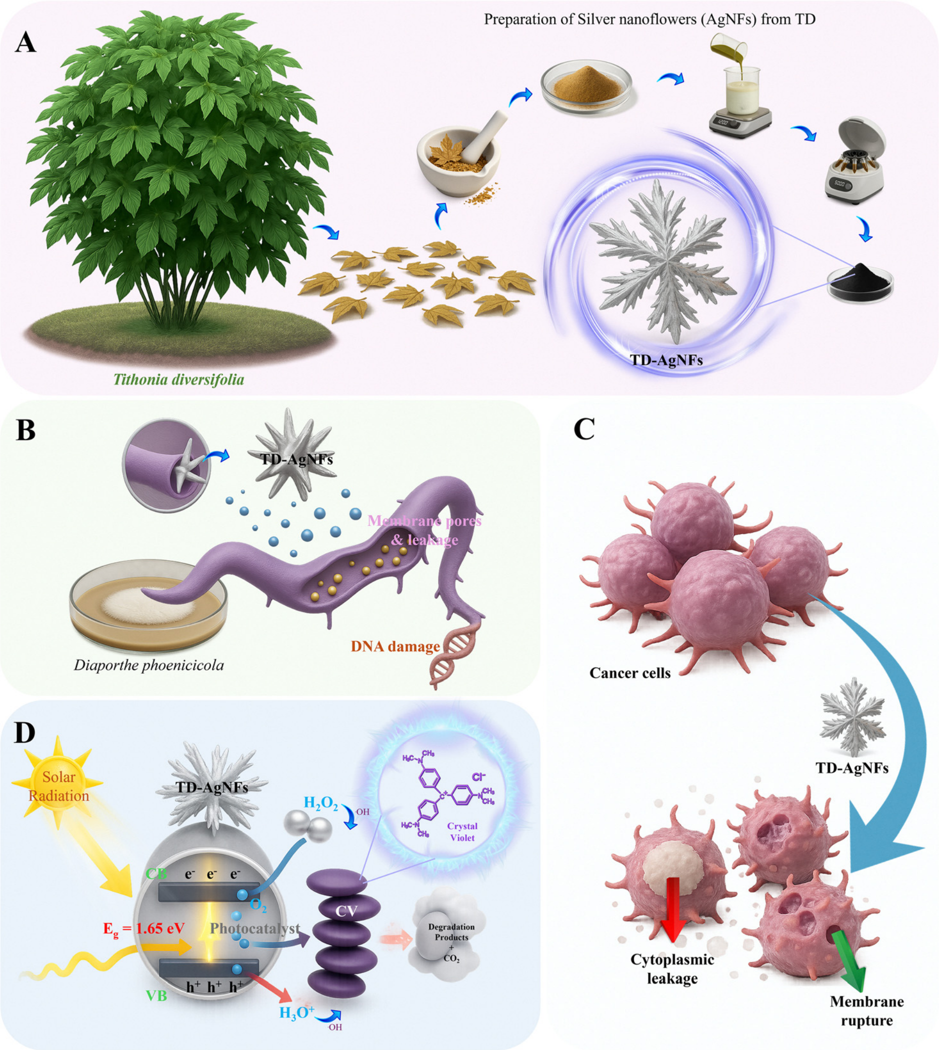

Fig. 1 Schematic of TD-AgNFs bio-synthesis to application. (A) Green synthesis from the *T. diversifolia* (TD) leaf extract. (B) Antifungal activity on *Diaporthe phoenicicola* with hyphal membrane disruption and leakage. (C) Anticancer activity with tumor cell membrane compromise and cell death. (D) Solar-driven photodegradation of crystal violet through plasmon-assisted interfacial interactions between TD-AgNFs and dye molecules.

plate-dominated, hierarchically assembled flowers rather than monodispersed spheres,[35] and provides optical signatures relevant to light-assisted photocatalytic studies, an anisotropic Ag morphology, and stable dispersion in aqueous media.

Building on the optical evidence, we recorded the FT-IR spectra of the aqueous leaf extract (TDLE, red) and the product (TD-AgNFs, blue), as shown in Fig. 2B, because FT-IR spectroscopy identifies the functional groups that drive reduction and remain as capping ligands. The TDLE spectrum shows a broad O–H stretch centered at ~3330 cm^{-1}, a weak aliphatic C–H stretch at ~2920 cm^{-1}, a strong band at ~1630 cm^{-1} assigned to the conjugated C═O and aromatic C═C of polyphenols, a feature at ~1380 cm^{-1} consistent with phenolic O–H bending and residual nitrate, and a C–O vibration at ~1050–1060 cm^{-1} attributable to alcohols and ethers in flavonoids and related metabolites.[36] Afterwards, the FT-IR spectrum of TDLE reveals the presence of hydroxyl, carbonyl, and amine functional groups, indicating the presence of polyphenols, flavonoids, and proteins responsible for the reduction and stabilization of Ag ions during NFs synthesis. After synthesis, the TD-AgNFs spectrum retains these organic signatures but shows diagnostic changes: the O–H region shifts and weakens toward ~3290 cm^{-1}, the ~1630 cm^{-1} band decreases and shifts to ~1605–1615 cm^{-1}, the ~1380 cm^{-1} band persists with altered intensity, and the ~1050–1060 cm^{-1} C–O band intensifies. New low-wavenumber features that are consistent with metal–ligand vibrations (Ag–O or Ag–N) appear in the ~620–560 cm^{-1} region. Taken together, the attenuation and shifts of O–H and carbonyl bands are consistent with the involvement of extract-derived functional groups during Ag^+ reduction, while the strengthened C–O signal and low-wavenumber metal–ligand features support the presence of organic surface capping on TD-AgNFs. This comparison supports the role of TDLE-derived functional groups in AgNFs formation and postsynthetic surface stabilization, which may contribute to aqueous dispersibility. Extending the FT-IR evidence for reduction and capping,

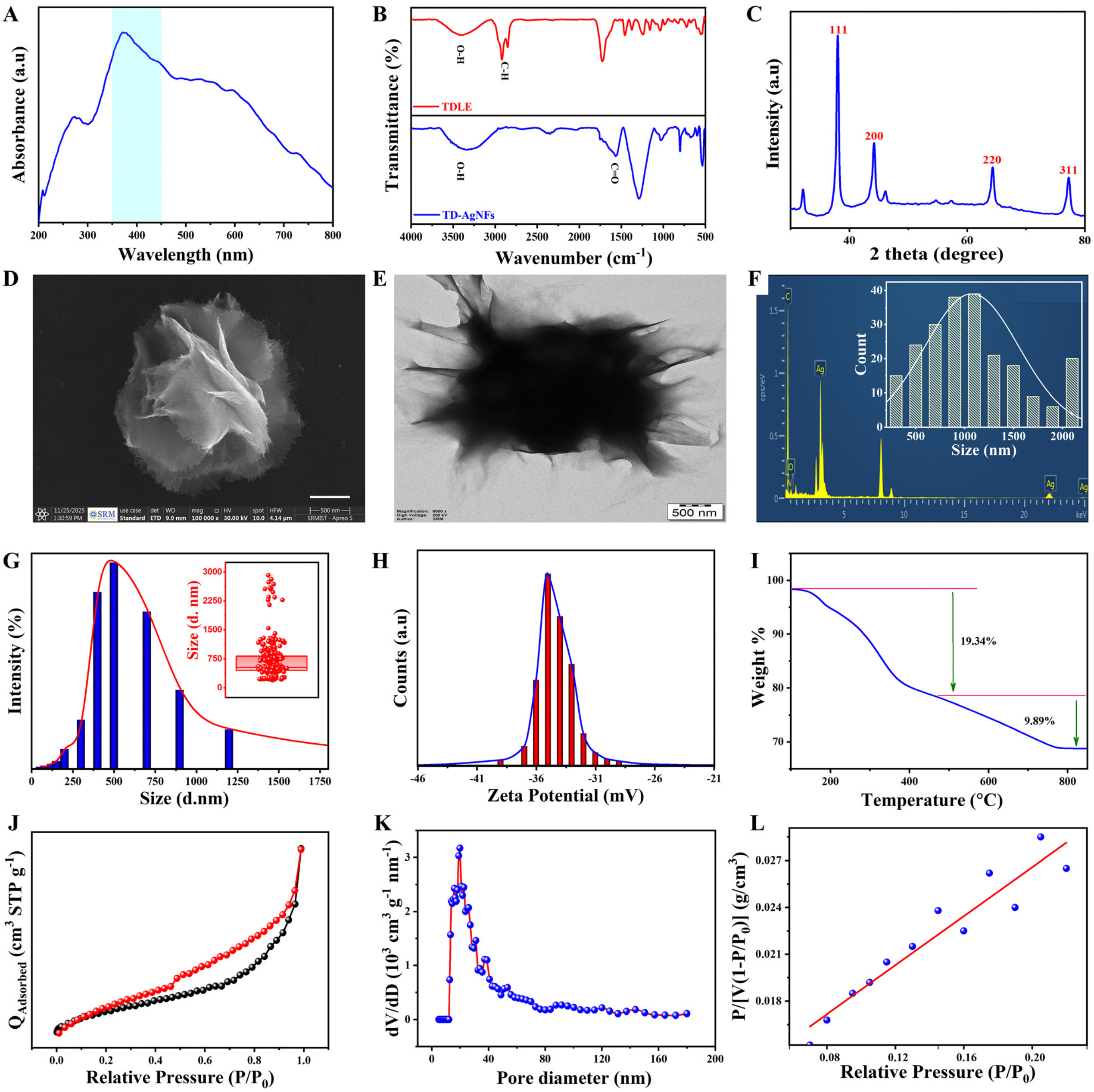

Fig. 2 Physicochemical characterization of the biosynthesized TD-AgNFs using TDLE. (A) UV-Vis absorption spectrum of TD-AgNFs showing the characteristic surface plasmon band (shaded region). (B) FT-IR spectra of (red) TDLE and (blue) TD-AgNFs after synthesis, highlighting the functional groups involved in reduction/capping. (C) XRD pattern of crystalline TD-AgNFs. (D) SEM micrograph revealing the flower-like hierarchical morphology. (E) TEM image of an individual TD-AgNFs. (F) EDS spectrum confirming the elemental composition; inset: particle/NF size distribution measured from TEM. (G) DLS hydrodynamic size distribution obtained on the same dispersion; inset: box-and-whisker plot of the size statistics. (H) Zeta-potential distribution of the TD-AgNFs colloid. (I) TGA curve of TD-AgNFs showing two main mass-loss events (values indicated). (J) Nitrogen adsorption–desorption isotherm at 77 K (BET), plotted as the adsorbed volume *versus* relative pressure P/P_0. (K) Pore size distribution derived from the desorption branch (BJH method). (L) BET plot, $P/[V(P_0 - P)]$ *versus* P/P_0, in the linear range used to calculate the specific surface area.

the powder XRD of the dried product confirms a predominantly metallic silver phase with high crystallinity (Fig. 2C). The distinct diffraction peaks at $2\theta \approx 38.05^\circ$, 44.34°, 64.19°, and 76.67° are indexed to the (111), (200), (220), and (311) planes of face-centered cubic (fcc) Ag, respectively, and are consistent with the standard silver pattern (JCPDS no. 00-001-1164).[36] The relatively strong reflection at $\sim 44^\circ$, corresponding to the (200)[7] plane, suggests a preferred orientation, which is commonly observed in platelet-rich silver architectures and is consistent with the observed morphology. Additional weak features in the $\sim 27^\circ$–57° region may arise from minor residual organic species and/or trace oxide-related contributions from the plant matrix; however, their low intensity does not alter the assignment of fcc Ag as the dominant phase. Five key crystallographic parameters—*i.e.*, crystallite size, interplanar spacing (*d*-spacing), lattice parameter, microstrain, and dislocation density—were calculated from the experimentally observed diffraction peaks, and the results are summarized in Table S2.

To further verify the anisotropic architecture and quantify lateral dimensions after the UV, FT-IR, and XRD analyses, we used high-resolution SEM. The SEM micrograph in Fig. 2D shows discrete flower-like superstructures composed of radially arranged, blade-like plates emerging from a compact core, with sharp petal edges and little evidence of sintering or collapse at the tips (scale = 10 μm).[37] Therefore, the term "NFs" is used in this study to describe the hierarchical flower-like assemblies formed by radially organized Ag platelets/petals rather than isolated spherical NPs. Elemental verification by SEM-EDS shows a uniform Ag distribution across the entire structure (Fig. S2B), and the corresponding spectrum reports dominant Ag L lines at ∼3 keV with no detectable extraneous elements; the quantification table lists Ag = 100 at%, within the instrument's detection limits. Together, these results confirm that the microscale architecture consists of radially assembled TD-AgNFs with clean, high-edge exposure and minimal contamination, a geometry that provides an abundant accessible surface for the biological and photocatalytic interfaces examined later.

Further, to resolve the internal architecture and verify the composition, we examined drop-cast TD-AgNFs dispersions by TEM at 200 kV. The TEM image in Fig. 2E shows a single, well-formed NFs with a dense central core and radially oriented, blade-like petals that are electron-transparent toward their tips. The strong mass–thickness contrast at the core and the tapered contrast along each petal indicate thin platelets that branch from a compact junction and terminate with sharp edges. Voids between adjacent petals create slit-like channels that are expected to act as mesoporous pathways during interfacial reactions. TEM analysis confirms the formation of hierarchical AgNFs composed of radially arranged petal-like platelets. The SAED pattern exhibits clear concentric rings, indicating the polycrystalline nature of the NPs. The diffraction rings are indexed to the (111), (200), (220), and (311) planes, consistent with the face-centered cubic (fcc) structure of metallic silver (JCPDS no. 00-001-1164). Minor differences between the SAED and XRD reflections can be attributed to the electron diffraction geometry and local crystallographic orientation.[38] The corresponding EDS spectrum in Fig. 2F confirms elemental silver as the sole detectable constituent, with an intense Ag Lα emission at ∼2.98 keV and high-energy Ag K lines at ∼22–25 keV. No other elemental signals rise above the background, which supports the high chemical purity of the product on the grid. The inset in Fig. 2F shows the lateral size distribution extracted from multiple individual flowers, centered at ∼1.0 μm, with measurements spanning from ∼0.5 to 2.0 μm, reflecting the natural variation in the petal number and extent within the hierarchical architecture. Together, the TEM image and EDS data verify the hierarchical flower-like assembly of thin silver platelets[39] radiating from a compact core, with clean surfaces and minimal inorganic impurities. This radial platelet/petal organization further supports the use of the term "NFs" for TD-AgNFs.

Further, we quantified the dispersion state because the surface charge and solvated size govern stability in media, contact with bacterial and mammalian membranes, and light-driven accessibility during photocatalysis. Electrophoretic measurements show a narrow zeta potential distribution centered modestly on the negative side, from around −29 to −40 mV at more negative values (Fig. 2H). Although the absolute zeta potential value shows electrostatic stabilization,[40] the FT-IR-identified phytochemical corona can provide steric and hydration barriers; therefore, the system is better described as possibly electrosterically stabilized. During photocatalysis, a stable colloid resists sedimentation, keeps active facets exposed to light, and minimizes dye self-aggregation artifacts. The dynamic light scattering result of the same dispersion yields an intensity-weighted mode in the submicrometer regime with a long tail extending to about 1.5–1.7 μm (Fig. 2G). The inset size box plot lies at ∼1.0 μm, which reflects the influence of larger objects on the intensity distribution.[41] These numbers are consistent with the electron microscopy observations when the measurement physics is considered. SEM reports dry-state lateral spans of whole flowers on the substrate that can reach tens of micrometers (Fig. S2A) because complete superstructures are immobilized and imaged after drying. TEM resolves individual flowers and thin petals on a grid with lateral sizes typically ranging from ∼0.5 to 2.0 μm (Fig. 2E and the histogram inset of Fig. 2F) after dispersion and drop-casting.[40] DLS, in contrast, measures the hydrodynamic diameter in a liquid, which includes the phytochemical shell and bound solvent. It also weights scattering intensity approximately with the sixth power of the particle size, so even a small fraction of larger bouquets or loose clusters strongly skews the intensity distribution to higher diameters. The anisotropic, plate-rich geometry further increases the apparent hydrodynamic size because rotational diffusion is slower than that for spheres, and orientation averaging broadens the peak. Differences in the sample state also matter. SEM and TEM probe dried objects, while DLS probes solvated ones at 25 °C in low-ionic-strength water, where the soft organic corona is fully extended. Taken together, Fig. 2G and H demonstrate that the *T. diversifolia*-derived capping imparts stable, near-neutral, electrosterically protected TD-AgNFs dispersions with hydrated sizes that map onto the microscopy-observed architecture, providing colloidal robustness. The zeta potential distribution (Fig. S2C) shows a single dominant peak, indicating a relatively uniform surface charge distribution on the NPs. The observed zeta potential value indicates strong electrostatic repulsion; therefore, the dispersion behaviour of TD-AgNFs is more appropriately attributed to electrosteric stabilization arising from the phytochemical capping layer rather than purely electrostatic stabilization.[42]

Thermal behaviour was evaluated to quantify the organic corona supplied by the leaf extract and to verify the robustness of the metallic core under heating (Fig. 2I). Under nitrogen at 10 °C min^{-1} from room temperature to 800 °C, the TD-AgNFs sample exhibits a clear two-step mass loss totalling ∼29.2%.[43] The first dominant step reaches ∼19.34% by about 450–500 °C and reflects the removal of physiosorbed and bound water, along with the volatilization and pyrolysis of low-molecular-weight phytochemicals that participate in reduction and remain on the surface after synthesis. A second slower step of ∼9.89% occurs between ∼500 °C and 800 °C, consistent with the decomposition and carbonization of more strongly adsorbed polyphenolic and carboxylate species that coordinate the Ag surface.[9] The observed total weight loss (29.23%) is attributed to the decomposition/desorption of surface-associated organic capping components, whereas the residual mass (70.77%) corresponds predominantly to the metallic silver fraction. Minimal additional mass loss above 500 °C indicates the good thermal stability of the synthesized AgNPs. For biological assays, the IC_{50} value was calculated using the total NP mass (metallic silver core + surface-associated organic capping components). The curve then approaches a plateau with a residual mass near 70%, which corresponds to the thermally stable metallic silver content and agrees with the FT-IR evidence of limited but persistent capping and with the EDS-confirmed purity. This profile indicates that the phytochemical layer constitutes roughly one-third of the total mass at most, that the organic fraction is stratified into weakly and strongly bound components, and that the inorganic framework remains intact without additional high-temperature events. Practically, the material tolerates common processing and sterilization temperatures, retains an active Ag surface after moderate heating, and preserves the ligand coverage that provides colloidal stability during the subsequent antibacterial, anticancer, and photocatalytic studies.

At last, textural analysis was performed because the catalytic rate, antimicrobial efficacy, and anticancer activity depend on the accessible surface area, density of exposed facets, and presence of mesoporous pathways that support rapid mass transport in aqueous media. In this context, the NFs architecture must provide abundant contact sites for dye molecules and for bacterial or mammalian cell interfaces while maintaining short diffusion paths through interpetal voids. To quantify these attributes, nitrogen adsorption–desorption measurements at 77 K were carried out on TD-AgNFs that had been degassed at 200 °C for approximately 3.3 h. The isotherm in Fig. 2J displays a clear type-IV profile with a pronounced hysteresis loop at a high relative pressure, a hallmark of mesoporous solids comprising slit and ink-bottle voids between stacked plates. The low-pressure region shows limited uptake, indicating minimal microporosity, while the progressive increase through intermediate pressures reflects the filling of mesoscopic channels created by the petal assembly. BET evaluation was performed on the adsorption branch within P/P_0 = 0.05–0.30.[44] The linear transform in Fig. 2L confirms the BET fitting region used for surface-area estimation. BET analysis yielded a specific surface area of 36.7 $m^2\ g^{-1}$, confirming the mesoporous textural features of TD-AgNFs. Pore metrics derived from a DFT kernel are shown in Fig. 2K. The total pore volume is 0.0787 $cm^3\ g^{-1}$, and the volume-mode pore diameter is around 40 nm, consistent with capillary condensation in interpetal gaps. The area-weighted mean diameter computed from D_4V/S = 4000 V_{tot}/S_BET is equal to ∼8.6 nm, which is smaller than the modal value, as expected, because the finest pores contribute disproportionately to the surface area. These quantitative results validate a hierarchically textured architecture with a substantial accessible area and robust mesoporous connectivity. In practical terms, the measured surface and pore network enrich the adsorption of crystal violet at active sites and speed up transport during sunlight exposure, which may contribute to the rapid degradation observed later. The same features increase the frequency of productive contacts with *Staphylococcus aureus* (SA) and *Pseudomonas aeruginosa* (PA), supporting possible interfacial redox interactions and Ag-based antimicrobial effects in water. For Huh7, THP-1, and SiHa models, the large density of edges and facets may enhance cell–surface interactions and contribute to the observed cytotoxic response. Taken together, Fig. 2J–L establish that the *T. diversifolia*-directed TD-AgNFs provide the surface-transport landscape required for high performance in both biomedical and photocatalytic applications, in full agreement with the anisotropic, petal-assembled morphology confirmed by TEM, SEM, FT-IR, XRD, TGA and SAED analyses.

2.2. Antioxidant function of TD-AgNFs

Oxidative stress underlies microbial persistence and tumor adaptation, so a material platform intended for antimicrobial, anticancer, and photocatalytic use should be evaluated for its interaction with reactive oxygen species in cells and in solution. The FT-IR and TGA results support the presence of extract-derived organic functionalities on the TD-AgNFs surface, while previous reports indicate that *T. diversifolia* leaves contain polyphenols, flavonoids, and related redox-active metabolites. With this foundation, TD-AgNFs were redispersed in water and examined for intracellular ROS moderation in SiHa cells using DCFDA. The peroxide control produced an intense green emission, whereas TD-AgNFs treatment yielded visibly attenuated fluorescence at 50 and 100 $\mu g\ mL^{-1}$, with the higher dose producing a stronger decrease (Fig. 3A). Quantification demonstrated a significant reduction in the mean fluorescence intensity relative to the oxidant control at both doses (Fig. 3B).[45] The behaviour may arise from the contributions of extract-derived surface functionalities and interfacial redox interactions at the petal-rich Ag surface. Solution-phase radical scavenging was then assessed with DPPH. TD-AgNFs displayed a monotonic dose response across 31.25–1000 $\mu g\ mL^{-1}$, increasing from roughly 22% inhibition at the lowest concentration to approximately 72% at the highest, with narrow error bars across replicates. The interpolation of the curve showed IC_{50} near 450 $\mu g\ mL^{-1}$ under these conditions (Fig. 3C).[46] The observed trend is consistent with contributions from the extract-derived surface layer and petal-rich architecture, which may increase accessible interfacial contact during radical-scavenging assays.

2.3. Anticancer and apoptosis-associated response of TD-AgNFs

Silver nanomaterials are widely reported to exhibit anticancer activity,[47] yet much of the prior work relies on chemically reduced colloids that aggregate in serum, require harsh

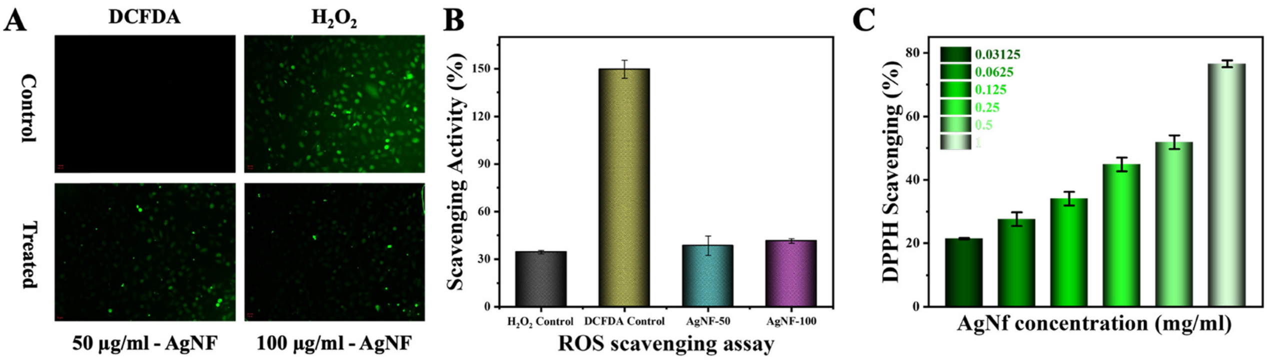

Fig. 3 Antioxidant and ROS-scavenging activity of TD-AgNFs. (A) DCFDA fluorescence micrographs of SiHa cells showing intracellular ROS under four conditions: untreated control, H_2O_2 control, H_2O_2 + AgNFs (50 µg mL^{-1}), and H_2O_2 + AgNFs (100 µg mL^{-1}); the lower green intensity indicates stronger ROS scavenging (scale bar = 100 µm). (B) Quantification of cellular ROS from DCFDA fluorescence for the same groups (mean ± SD, n = 3). (C) DPPH radical-scavenging activity of AgNFs across a two-fold dilution series from 31.25 to 1000 µg mL^{-1} (mean ± SD, n = 3).

stabilizers, or display nonselective toxicity with mixed apoptosis and necrosis readouts.[48] Reported limitations include poor dispersion stability during exposure, broad size distributions that blur dose response, and surface chemistries that either quench activity or trigger off-target oxidative bursts.[49] The presented design addresses these deficits by using a plant-directed route to hierarchically petal-like TD-AgNFs capped by *T. diversifolia* metabolites. Building directly on this rationale, THP-1 (suspension), Huh7, and SiHa (adherent) cultures were exposed for 24 h to a graded TD-AgNFs series spanning from 31.25 to 1000 µg mL^{-1}, and metabolic viability was quantified by the MTT assay. The synthesized silver nanomaterials exhibit concentration-dependent cytotoxicity, with cell viability decreasing as the treatment concentration increases across the tested cancer cell models. Capecitabine served as the positive control for assay validation. The TDLE also shows measurable cytotoxicity, indicating the intrinsic bioactivity of the extract. Silver nitrate produces pronounced cytotoxicity in the MTT assay, consistent with the rapid and nonspecific damage induced by free Ag^+ ions. In contrast, the TD-AgNFs show a concentration-dependent reduction in cancer cell viability in the investigated models, which may be associated with Ag-based surface effects, possible Ag^+ contribution, and phytochemical capping-mediated cell interactions.

The dose–response results in Fig. 4A–E show a monotonic decrease in viability in all three models, with tight replicate

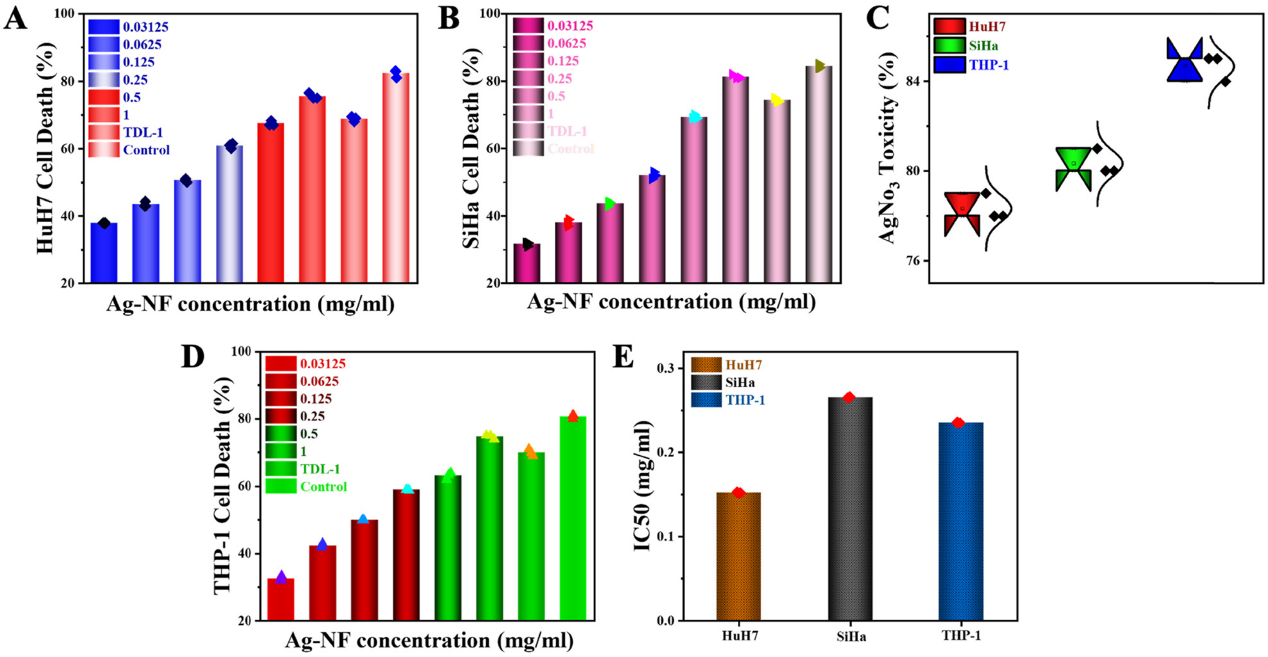

Fig. 4 Dose-dependent anticancer activity of TD-AgNFs measured by the MTT assay after 24-h exposure. (A) Huh7, (B) SiHa, and (D) THP-1 cell responses across TD-AgNFs concentrations (31.25–1000 µg mL^{-1}). Cell death (%) was calculated relative to untreated controls. (C) $AgNO_3$ control treated with SiHa, Huh7, and THP-1 cell lines. Error bars indicate mean ± SD, n = 3 independent experiments. (E) Summary of IC_{50} values obtained from the dose–response curves: Huh7 ≈ 160 µg mL^{-1}, THP-1 ≈ 230 µg mL^{-1}, and SiHa ≈ 260 µg mL^{-1}.

variance and stable vehicle controls. The working range brackets the transition to strong cytotoxicity, consistent with IC_{50} values near 230 µg mL^{-1} for THP-1, 160 µg mL^{-1} for Huh7, and 260 µg mL^{-1} for SiHa under these conditions. The reduced MTT signal indicates decreased metabolic activity and loss of cell viability in NP-treated cancer cells.[50] Differences in the slopes of the hematologic and adherent models align with the contact geometry. Suspension cells experience frequent whole-cell encounters with dispersed petals, whereas adherent monolayers present broad membrane areas along which petal edges can spread, enabling sustained interfacial contact and uptake at higher doses. Extending these population-level trends, matched AO/EB fluorescence microscopy was used to examine live/dead staining patterns and apoptosis-associated morphological changes. Control fields show predominantly green, morphologically intact nuclei, whereas TD-AgNFs exposure yields abundant ethidium-positive nuclei with bright orange-red emission,[51] together with chromatin condensation, nuclear fragmentation, and late apoptotic bodies, increasing with the dose (Fig. 5A–C). The merged images display progressive orange overlays at higher concentrations, consistent with the transition from early-to-late apoptosis and secondary necrosis. These imaging phenotypes align with the MTT results and support an apoptosis-associated cytotoxic response in TD-AgNF-treated cancer cells, while the petal-rich architecture and phytochemical capping may contribute to enhanced cell–material interactions.[52]

2.4. Regulation of cancer cell migration by TD-AgNFs

Cell migration in malignant monolayers is a proxy for metastatic potential and tissue remodeling, yet prior NP-based studies often report conflicting outcomes. Chemically reduced AgNPs frequently aggregate in serum, rely on harsh surfactants, and trigger excessive oxidative stress, which suppresses migration

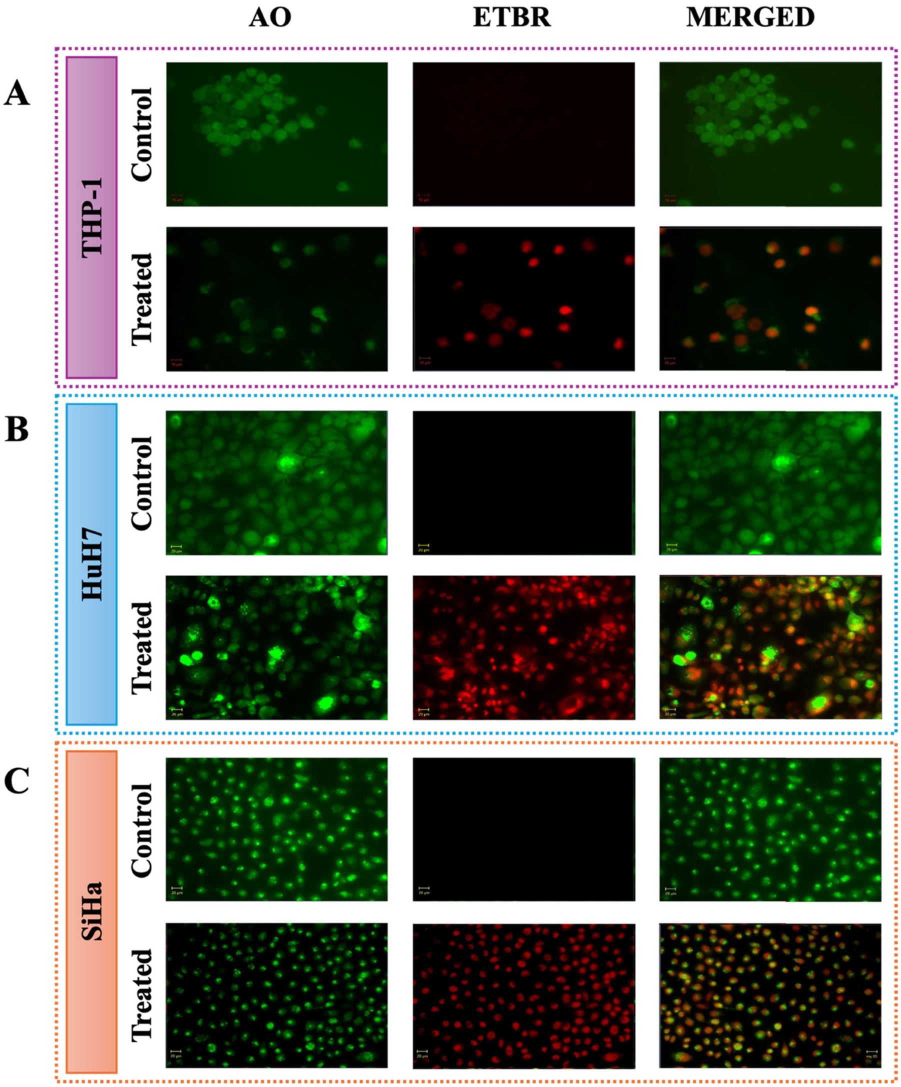

Fig. 5 AO/ETBR fluorescence microscopy images of apoptosis in (A) THP-1, (B) Huh7, and (C) SiHa cells after exposure to TD-AgNFs. For each cell line, the top row shows control cells, and the bottom row shows TD-AgNFs (125 and 250 µg mL^{-1})-treated cells (24 h, indicated concentration). Columns show AO, ETBR, and merged images. Scale bars = 10 µm.

or confounds interpretation by coupling cytotoxicity to the observed migration inhibition.[53] Reports also note broad size dispersity and unstable coronas that change during the assay window, producing variable edge dynamics and irreproducible gap kinetics.[54] The presented TD-AgNFs platform was selected to avoid these pitfalls. The green synthesis furnishes a phytochemical corona that stabilizes the colloid in aqueous media and moderates the redox pressure at the doses used for migration studies. The petal-like architecture provides abundant exposed facets that may influence cell–material interactions at the scratch boundary. The expectation was the prevention of closure at a biologically tolerable dose window, without the confounding effects typical of unstable or strongly pro-oxidant suspensions.

Building on this rationale, scratch assays were performed on confluent SiHa and Huh7 cancer cell monolayers using an identical timeline, and the working TD-AgNFs dose was applied immediately after scratch creation. Representative phase-contrast sequences document the evolving gap. In Fig. 6A (SiHa) and Fig. 6C (Huh7), untreated controls show the progressive narrowing of gaps due to cancer cell migration at intermediate times. TD-AgNF-treated fields display visibly straighter fronts and stunted cell migration at corresponding time points at the terminal frame. Quantification of percent migration is summarized in Fig. 6B and D. Treated groups show poor cell migration compared to time-matched controls at later points of the assay, and the statistical markers indicate significance in Huh7 ($p < 0.0001$, ****) and SiHa ($p < 0.05$, *) within the same schedule. Replicates exhibit tight variance, consistent with stable dispersion and uniform coverage during incubation.

These observations suggest that the plant-derived surface layer and petal-rich morphology may contribute to reduced cancer cell motility under the tested *in vitro* conditions. The near-neutral, electrosterically stabilized, dispersed, plate-rich petals may affect cell-front progression at the scratch rim. Within this dose window, the balance prevents migration and closure, pushing the cellular response toward stress and growth arrest, a trend consistent with the MTT and AO/EB outcomes in cancer cell viability.

2.5. Transwell migration assay

The migratory behavior of SiHa and Huh7 cells following treatment with TD-AgNFs was evaluated using a transwell migration assay.[55] Transwell inserts (8.0 μm pore size, 24-well format) were used. Cells were serum-starved, harvested, and resuspended in a serum-free medium, and 5×10^5 cells were seeded in the upper chamber of each insert and treated with TD-AgNFs (50 μg mL^{-1}). The lower chamber was filled with the complete culture medium containing 10% fetal bovine serum (FBS) as a chemoattractant. Cells were incubated for 24 h at 37 °C in a humidified atmosphere with 5% CO_2. After incubation, nonmigrated cells on the upper surface of the membrane were gently removed using a cotton swab. Migrated cells on the lower surface were fixed with 4% paraformaldehyde and stained with crystal violet. The stained cells were visualized using an inverted optical microscope and quantified by counting five randomly selected fields per membrane. Cell migration was expressed relative to the untreated control group. Representative images of untreated and TD-AgNF-treated SiHa and Huh7 cells are shown in Fig. 7A–C, respectively.

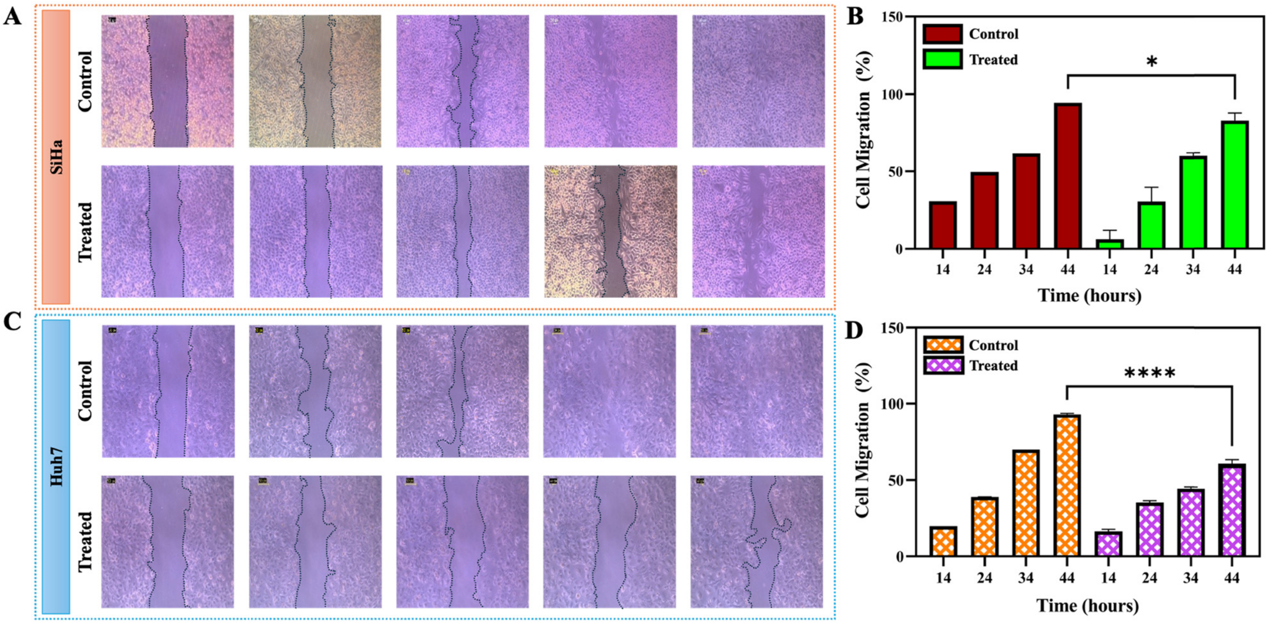

Fig. 6 Scratch-wound assay showing the inhibition of cancer cell migration by TD-AgNFs. Representative phase-contrast images of wound closure in (A) SiHa and (C) Huh7 cells under control and TD-AgNF-treated conditions (50 μg mL^{-1}); dotted lines indicate wound edges at each time point. Quantification of cell migration (%) for SiHa (B) and Huh7 (D). Data are presented as mean ± SD (n = 3 independent experiments). Statistical significance was determined by one-way ANOVA with Tukey's *post hoc* test ($p < 0.05$ and ****$p < 0.0001$).

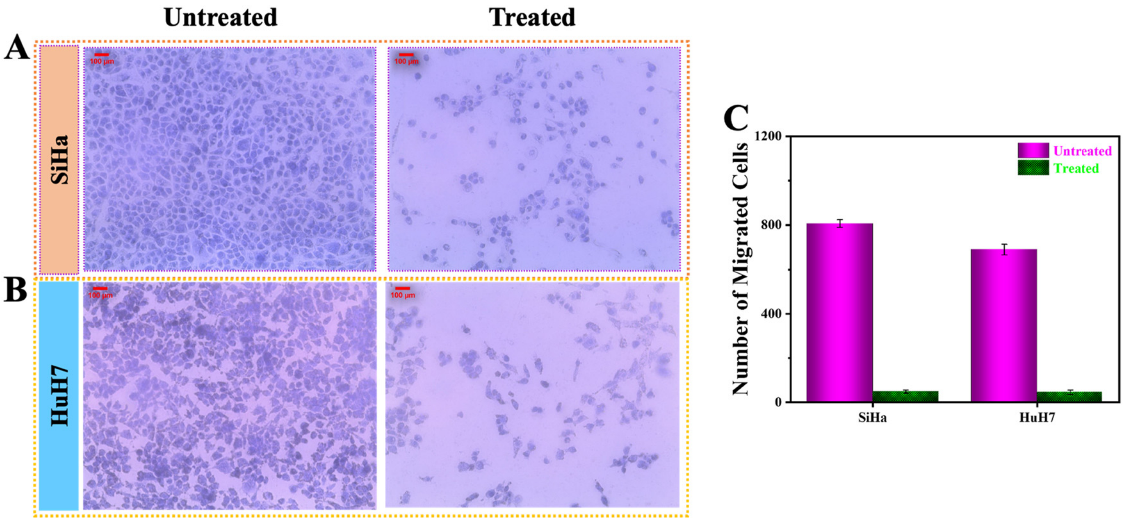

Fig. 7 Transwell migration assay of TD-AgNFs. (A) Untreated and 50 µg mL^{-1} AgNF-treated phase-contrast images of SiHa cells. (B) Untreated and 50 µg mL^{-1} AgNF-treated phase-contrast images of Huh7 cells. (C) Data are presented as mean ± SD (*n* = 3 independent experiments). AgNFs significantly reduced the migration of SiHa and Huh7 cells through the transwell membrane.

2.6. Dose-responsive antimicrobial screening of TD-AgNFs

Effective control of phytopathogenic fungi and clinically relevant bacteria remains difficult because many NP formulations aggregate in rich media, rely on harsh capping agents, or deliver bursts of oxidative stress that compromise host safety while giving erratic readouts.[56] The literature on chemically reduced AgNPs often reports variable zones of inhibition and poor reproducibility once serum proteins or polysaccharides adsorb to the surface.[57] The *T. diversifolia* route was adopted to overcome these limitations. Phytochemical ligands from the extract stabilize the AgNFs in aqueous media and contribute intrinsic antimicrobial functionality through phenolic and terpenoid groups, while the petal-like high-area architecture supports sustained Ag$^+$ release and dense interfacial contact with microbial envelopes. The resulting construct is expected to suppress colony expansion and produce dose-responsive inhibition in disk and plate assays without the confounding effects of unstable coronas.

Fungal inhibition was tracked against *Diaporthe phoenicicola* on PDA. A seven-day series of plates was used to document colony expansion in the blank control with the antifungal reagent amphotericin-B (5 mg mL^{-1}) and in TD-AgNFs treatments at 5 and 10 mg mL^{-1}. The montages in Fig. 8A show progressive radial growth in the control, which reaches near-confluence by day 7, whereas both TD-AgNFs doses restrict mycelial advancement and preserve a smaller colony disc throughout the experiment, with the 10 mg mL^{-1} dose giving the strongest suppression. The quantification in Fig. 8B confirms a consistent, day-by-day divergence between the control trajectory and the treated groups. The trend matches expected

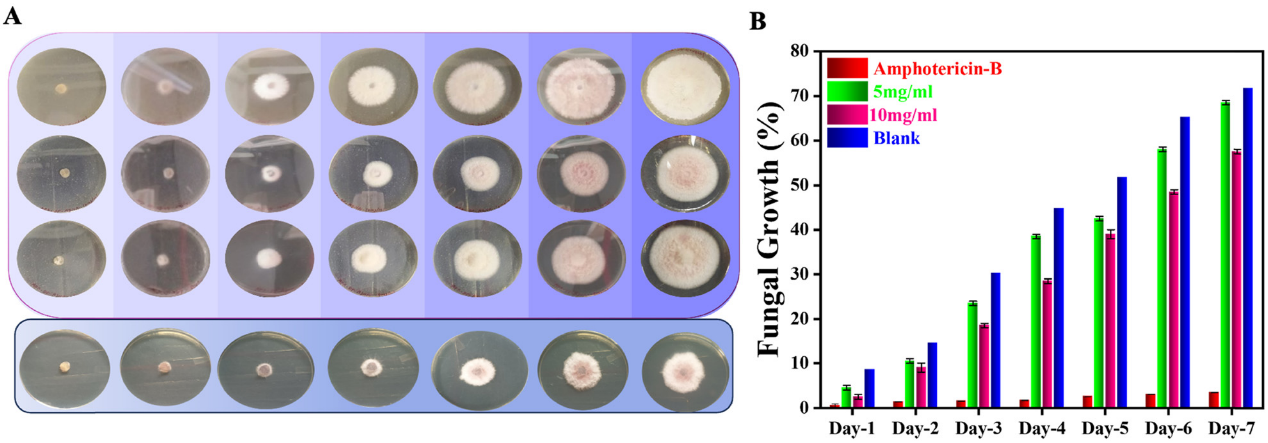

Fig. 8 Time-dependent antifungal activity of TD-AgNFs against *Diaporthe phoenicicola* potato dextrose agar (PDA) at different incubation times, calculated using the disk diffusion method. (A) Representative PDA plates imaged from day 1 to day 7 under control and TD-AgNFs treatment conditions (5000 and 10 000 µg mL^{-1}). (B) Quantification of fungal growth (%) over time for the control, 5000 µg mL^{-1}, and 10 000 µg mL^{-1} groups. Bars represent mean ± SD (*n* = 3 independent plates).

Ag-mediated antifungal mechanisms that include the disruption of membrane integrity, binding to thiol-containing enzymes, interference with ergosterol-rich domains, and oxidative damage to hyphal tips.[58] The plant-derived corona likely augments this response by maintaining dispersion near the colony edge and by delivering phenolic groups that perturb the redox balance at the hyphal surface.

Bacterial activity was assessed by disk diffusion against SA and PA as a zone-of-inhibition-based antimicrobial screening assay. Because the present antibacterial evaluation was based on disk diffusion, the results are interpreted as dose-responsive inhibition zone evidence rather than MIC/MBC-based bacteriostatic or bactericidal quantification. The representative plates in Fig. 9A, B display clear, circular inhibition zones for TD-AgNFs loadings of 1.25, 2.5, 5, and 10 mg per disk. The solvent control shows no zone, whereas the antibiotic control (AB) gives the expected strong clearance. The dose–response bar charts in Fig. 9C show increasing zone diameter with the TD-AgNFs dose for both organisms. SA exhibits larger zones than PA at the same doses, consistent with the higher intrinsic permeability of Gram-positive envelopes and the known multidrug defenses of PA.[59] The data indicate a dose-responsive antibacterial effect that may arise from the combined interfacial contributions of the NF architecture, Ag-based surface activity, and *T. diversifolia*-derived phytochemical capping. The petal-rich morphology may improve contact with bacterial envelopes, while the phytochemical shell may help preserve dispersion during the assay window.

2.7. Sunlight-assisted photocatalytic degradation of crystal violet by TD-AgNFs

Industrial dye effluents remain difficult to remediate under natural light because many photocatalysts demand UV irradiation, lose activity through rapid e$^-$/h$^+$ recombination, or aggregate in water so that only a small fraction of surface sites participate in the reaction.[60] Silver colloids can interact with visible light through localized surface plasmon resonance, but conventional, chemically capped particles often suffer from solvent-induced agglomeration, unstable surface chemistry, and surface passivation, which can reduce catalytic accessibility and slow dye degradation.[61] The TDLE route was chosen to overcome these bottlenecks. The plant matrix furnishes a thin phytochemical corona that stabilizes the TD-AgNFs in water, preserves access to active facets, and promotes the adsorption of cationic dyes through polar and π interactions (Fig. 1). The petal-like morphology supplies exposed edges and surface sites that may improve light-assisted interfacial interactions under sunlight, and the mesoporosity and high area quantified earlier enhance mass transfer at the solid–liquid interface. In combination, these features were designed to achieve the fast, visible-light degradation of crystal violet (CV) without sacrificial agents or harsh processing.

Consistent with this design, time-resolved UV-vis spectra showed a steady attenuation of the CV absorption band at $\sim$585 nm when TD-AgNFs were dispersed in water and exposed to sunlight (Fig. 10A). Control experiments showed no significant change in the characteristic CV absorption band in the absence of sunlight or in the absence of TD-AgNFs, confirming that neither dark adsorption nor direct photolysis contributed appreciably to dye removal under the applied conditions. In contrast, a pronounced decrease in absorbance was observed only under sunlight irradiation in the presence of TD-AgNFs, demonstrating a catalyst-driven photocatalytic process. The TD-AgNFs showed a slower decline in the CV band intensity (Fig. 10B), while the dye-only control remained essentially unchanged, further supporting a catalytic rather than photolytic mechanism. End-point comparisons (Fig. 10C) revealed a clear concentration dependence: lower initial CV loads (5–10 ppm) were removed more efficiently than higher loads (20–25 ppm), reflecting reduced inner-filter effects and better catalyst accessibility. The visual series in Fig. S3A–E mirrors the spectral data; purple solutions with TD-AgNFs fade to nearly colorless most rapidly for the aqueous dispersion.[62]

Kinetic fitting to $\ln(C_0/C_t) = k_{\mathrm{app}}t$ returns pseudo-first-order behaviour with larger k_{app} values for water-dispersed TD-AgNFs and for lower starting concentrations, consistent with a catalyst-assisted dye-degradation process. Under solar irradiation, the plasmonic Ag surface and petal-rich morphology may

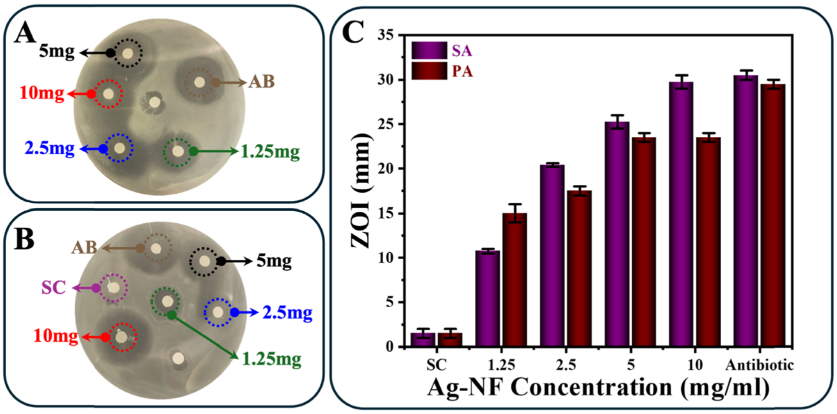

Fig. 9 Dose-dependent antibacterial activity of TD-AgNFs in a disk diffusion assay. (A) Representative agar plate for *Staphylococcus aureus* (SA) and (B) *Pseudomonas aeruginosa* (PA), showing zones of inhibition at 1250, 2500, 5000, and 10 000 µg mL^{-1}, with the antibiotic control (AB) and solvent control (SC). (C) Quantification of the zone of inhibition (ZOI, mm) for SA and PA. Bars represent mean ± SD (n = 3).

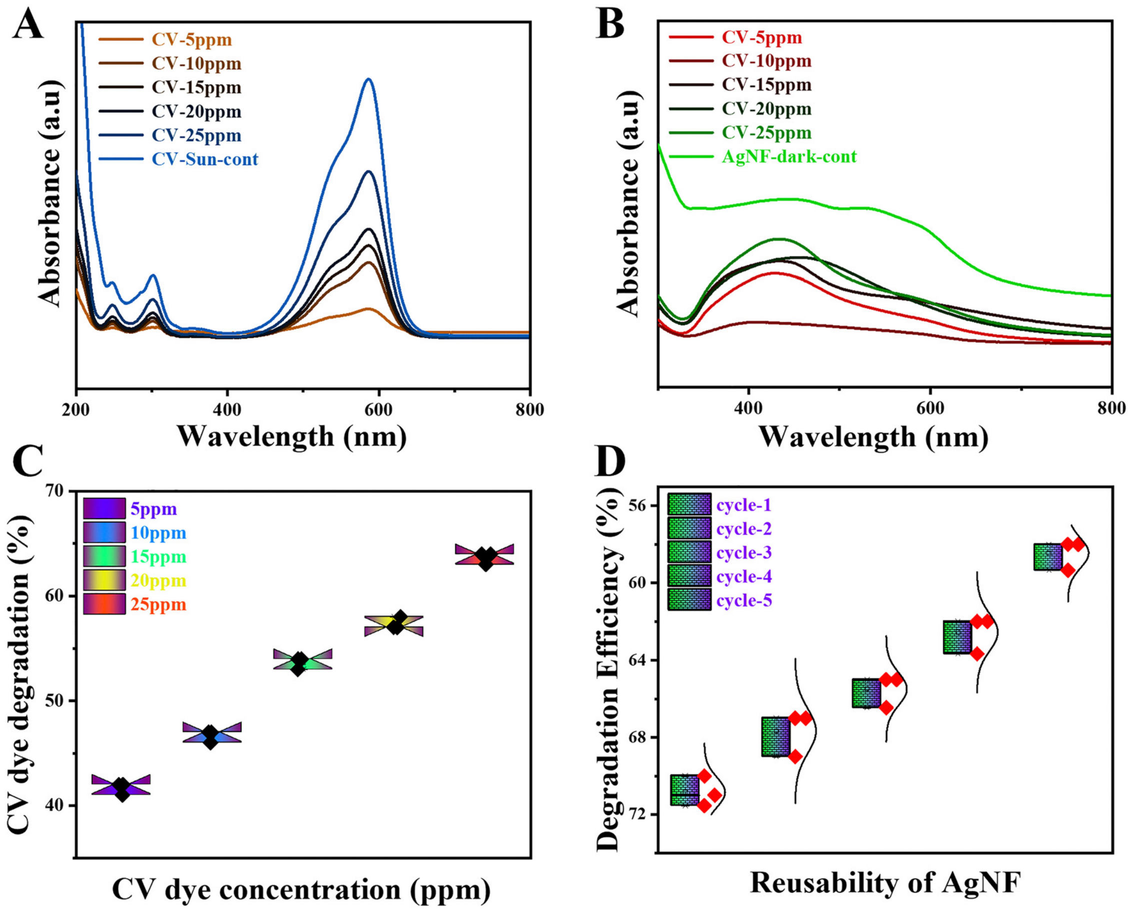

Fig. 10 Sunlight-assisted photocatalytic degradation of crystal violet (CV) using TD-AgNFs. (A) UV-Vis absorbance spectra (200–800 nm) of CV at different initial concentrations (5–25 ppm) after sunlight irradiation in the presence of TD-AgNFs, including the sunlight control (CV-Sun-cont). (B) Corresponding spectra under dark control conditions (AgNF-dark-cont). (C) Percentage CV degradation as a function of the initial CV concentration. (D) Reusability of TD-AgNFs over five consecutive cycles, showing retained degradation efficiency.

facilitate interfacial charge-transfer processes and dye–catalyst interactions. These processes can contribute to the progressive decrease in the crystal violet absorption band and the formation of less-absorbing photoproducts.[63] The phytochemical shell from *T. diversifolia* keeps the petals dispersed, moderates nonproductive recombination, and assists dye preconcentration at the interface, whereas ethanol may alter dye–catalyst interactions and reduce the apparent degradation rate. The reusability of TD-AgNFs was further evaluated during the photocatalytic degradation of CV (25 ppm) under visible-light irradiation (Fig. 10D and Fig. S3D). The catalyst retained appreciable photocatalytic activity over successive reuse cycles, indicating good operational stability. The sustained performance after repeated recovery and reuse suggests that TD-AgNFs remain catalytically active under the applied reaction conditions, supporting their potential for further evaluation in dye-contaminated water treatment studies.

3. Conclusion

This study demonstrated the green, single-pot, aqueous synthesis of hierarchically structured AgNFs using TDLE as a biogenic reducing and stabilizing medium. Spectroscopic and microscopic characterizations supported the formation of flower-like Ag assemblies with phytochemical surface capping, fcc crystallinity, a petal-like morphology, and mesoporous textural features. FT-IR, TGA, SEM, TEM, XRD, zeta potential, DLS, and BET analyses collectively confirmed the structural, surface, and textural characteristics of the TD-AgNFs. The material showed dose-responsive antibacterial activity against *Staphylococcus aureus* and *Pseudomonas aeruginosa*, antifungal activity against *Diaporthe phoenicicola*, and concentration-dependent anticancer activity in Huh7, THP-1, and SiHa cancer cell models, with IC_{50} values of 160, 230, and 260 μg mL^{-1}, respectively. AO/EB staining and intracellular ROS imaging further supported a treatment-dependent cytotoxic response with possible oxidative-stress-associated contributions. Scratch and transwell assays indicated the *in vitro* antimigratory activity of TD-AgNFs under the tested conditions. In addition, TD-AgNFs enabled sunlight-assisted crystal violet degradation across 5–25 ppm, based on UV-vis absorbance changes. Overall, the results support TD-AgNFs as a plant-derived hierarchical Ag nanostructure with promising *in vitro* biomedical activity and sunlight-assisted dye-degradation performance.

4. Materials and methods

4.1. Materials and chemicals

Silver nitrate ($AgNO_3$), Dulbecco's modified Eagle's medium (DMEM), Roswell Park Memorial Institute (RPMI) 1640 medium, trypsin–EDTA, fetal bovine serum (FBS), sodium bicarbonate, antibiotic solution, 3-(4,5-dimethylthiazol-2-yl)-2,5-diphenyltetrazolium bromide (MTT), acridine orange, ethidium bromide, crystal violet dye, hydrogen peroxide (H_2O_2), and 2′,7′-dichlorofluorescein diacetate (DCFDA) were obtained from Sigma-Aldrich (St. Louis, MO, USA). The human monocytic leukemia cell line THP-1, cervical carcinoma cell line SiHa, and hepatocellular carcinoma cell line Huh7 were sourced from the National Centre for Cell Science (NCCS), Pune, India.

4.2. Preparation of TDLE

Fresh leaves of *T. diversifolia* were collected from Potheri, Chennai, India, during February–May 2025, corresponding to the late winter to premonsoon season in Tamil Nadu. The collected leaves were thoroughly rinsed with distilled water to remove surface impurities and shade-dried at room temperature for 7–10 days until fully dehydrated. The dried leaves were milled to a fine powder and stored in airtight containers until use. Fig. S1A shows the extract preparation: 10 g of the dried leaf powder was mixed with 200 mL of sterile distilled water, corresponding to a powder-to-solvent ratio of 1 : 20 (w/v) or 50 mg mL^{-1}. The mixture was heated to a gentle boil for 10 min to facilitate phytochemical release.[64] After cooling to room temperature, the mixture was filtered through Whatman filter paper to obtain a clear TDLE, which was stored at 4 °C until use.

4.3. Synthesis of TD-AgNFs

TD-AgNFs were synthesized (Fig. S1B) by adding 10 mL of TDLE dropwise to 90 mL of 1 mM $AgNO_3$ under constant stirring at room temperature. The formation of NFs was monitored visually by a color change from pale yellow to dark brown, typically within 30 min. The colloid was collected by centrifugation at 12 000 rpm for 20 min at 10 °C, washed with distilled water, and resuspended for subsequent characterization and biological evaluation.

4.4. Physicochemical characterization

The characterization of the TDLE and the resulting TD-AgNFs encompassed optical, vibrational, structural, morphological, interfacial, thermal, and textural analyses. The UV-vis absorption spectra of the extract and the NFs were collected on a UV-3600Plus Series spectrophotometer (model: UV3600) using UV Probe software (Version 2.70) in the absorbance mode over the range of 190–800 nm, and the data were processed and visualized in Origin Pro 2018 to assess optical properties and plasmonic behaviour. FT-IR spectra were acquired on a Shimadzu IRTracer-100 FT-IR spectrophotometer controlled by LabSolutions over the range of 5000–500 cm^{-1} to identify the functional groups associated with the phytochemical capping of the silver surface. X-ray diffraction patterns of a representative batch of TD-AgNFs were recorded on a diffractometer (model: 207756) operated in the continuous scan mode with a fixed divergence slit using a copper anode across the 2θ range of 5.01°–99.98° with a step size of 0.022°. Diffractograms were processed at LabSolutions to evaluate the crystal structure, phase purity, and average crystallite size. The morphology and elemental composition were examined by high-resolution scanning electron microscopy with energy-dispersive X-ray spectroscopy (HR-SEM/EDX; JEOL, Japan) and by high-resolution transmission electron microscopy with EDX and SAED (HR-TEM/EDX; JEOL JEM-2100 Plus, JEOL, Japan). Hydrodynamic size distributions and surface zeta potentials were measured on a dynamic light scattering-based instrument using disposable sizing cuvettes at 25.0 °C, with a dispersant refractive index of 1.330, a material refractive index of 1.59, and a typical count rate of 60 kcps, yielding parameters relevant to colloidal stability and dispersion behaviour. Thermal properties and compositional stability were assessed by simultaneous thermal analysis using an STA 2500 REGULUS TGA-DSC thermal analyzer, with data acquisition and interpretation performed using the instrument's proprietary software. The specific surface area and porosity were determined by nitrogen adsorption–desorption on an Autosorb iQ Station 2 after outgassing 0.0081 g of a sample at 200 °C for approximately 3.3 h. Measurements were conducted in the standard mode at a bath temperature of 77.35 K. Helium was used for void-volume calibration in a 6 mm cell. Data reduction accounted for thermal transpiration using an effective molecular diameter of 3.54 Å and a cell stem diameter of 4.00 mm. Nitrogen properties were set to a molecular weight of 28.013, a molecular cross-sectional area of 16.2 Å^2, and a liquid nitrogen density of 0.808 g cm^{-3} to compute the BET surface area and related textural parameters.

4.5. Biological applications

Green, plant-derived nanomaterials are increasingly explored to mitigate free-radical and microbe-driven pathologies and to reduce dose-limited toxicities associated with conventional chemotherapy.[21] Accordingly, the biological performance of TD-AgNFs was evaluated using anticancer, live/dead discrimination, migration (wound healing), antimigration activity (transwell migration assay), antibacterial, antifungal, antioxidant (DPPH), intracellular ROS, and photocatalytic dye degradation assays, as detailed below.

4.5.1. Anticancer activity: MTT assay. Cytotoxicity was assessed by the MTT colorimetric assay in THP-1 (human monocytic leukemia; suspension), Huh7 (human hepatocellular carcinoma; adherent), and SiHa (human cervical carcinoma; adherent) cell lines in 96-well plates. For adherent lines (Huh7 and SiHa), the cells were seeded and allowed to attach for 24 h prior to treatment; THP-1 cells were directly seeded and treated. Cells were exposed to graded concentrations of TD-AgNFs from 31.25 to 1000 μg mL^{-1} for 24 h at 37 °C and 5% CO_2. A MTT working solution (500 μg mL^{-1} in PBS; 100 μL per well) was added and incubated for 4 h to form formazan. Supernatants were removed carefully, DMSO (100 μL per well) was added to solubilize formazan, and absorbance was read at 570 nm on a microplate reader. Cell viability (%) was calculated as follows:

$(A_{\text{treated}}/A_{\text{control}}) \times 100$; cell death (%) = 100 − viability (%).[65] Capecitabine was used as the standard positive control, and the plant extract alone was employed as the plant control to systematically evaluate and benchmark the anticancer efficacy of the biosynthesized silver nanomaterials. IC_{50} values were estimated by fitting the concentration–response data. When a linear fit was used, the relation $y = mx + c$ (m and c from the death graph) was solved at $y = 50$ to obtain the concentration corresponding to 50% viability.[65] All experiments were performed in triplicate, and data are presented as mean ± SD, with $p < 0.05$ considered significant.

4.5.2. AO/EB live–dead staining. Live/dead discrimination followed established AO/EB staining procedures.[66] Sterile glass coverslips were placed in 6-well plates; cells (1×10^4 cells per well) were seeded in a complete medium and incubated for 24 h (37 °C, 5% CO_2) to allow adhesion. The medium was then replaced with a fresh medium containing TD-AgNFs stock dispersions equivalent to final exposure concentrations of approximately 125 and 250 μg mL^{-1} and incubated for the required period. Coverslips were stained in the dark for 30 min at room temperature using acridine orange (100 μL) and ethidium bromide (40 μL) in 2 mL of PBS, washed twice with 1× PBS, and imaged immediately by confocal microscopy (LSM-700, Carl Zeiss, Germany).[65] Live cells emitted green fluorescence (≈526 nm), and dead cells emitted red fluorescence (≈630 nm); images were acquired with constant settings.

4.5.3. Antimigratory (scratch) assay in SiHa and Huh7. Cancer cell migration was evaluated by an *in vitro* scratch assay.[18] Huh7 and SiHa cells were seeded in 12-well plates (2 mL of DMEM per well) to achieve near confluence after 24 h.[53] A uniform scratch was introduced with a sterile pipette tip, media were replaced with DMEM containing TD-AgNFs (50 μg; as specified), and control wells received DMEM alone. Scratch closure was imaged at 14, 24, 34, and 44 h post-treatment using an inverted microscope. The width of the scratch was quantified at each time point, and percent closure was calculated as follows: $[(W_0 - W_t)/W_0] \times 100$.

4.5.4. Transwell migration assay. The migratory behaviour of SiHa and Huh7 cells was assessed using a transwell migration model. Treatment with AgNFs (TD-AgNFs, 50 μg mL^{-1}) significantly reduced the number[67] of migrated cells compared to untreated controls after 24 h. Fig. 7A–C show the pronounced decrease in cell migration, indicating that TD-AgNFs effectively suppress cancer cell motility under serum-gradient conditions.[68] This inhibitory effect suggests that TD-AgNFs may interfere with migration-associated cellular processes under the tested conditions.

4.5.5. Antibacterial activity. Antibacterial effects against *Pseudomonas aeruginosa* and *Staphylococcus aureus*[55] were measured by the disk-diffusion method following a standard protocol with minor modifications.[56] TD-AgNFs dispersions of 1250, 2500, 5000, and 10 000 μg mL^{-1} were used for disk-diffusion testing, with the same loading volume applied to each disk. A solvent control and a standard antibiotic disk (positive control; chloramphenicol) were included. Plates were incubated under standard conditions, and zones of inhibition (mm) were recorded. Where applicable, percent inhibition was calculated as follows: $((C - T)/C) \times 100$, with C and T defined by the relevant control and treated growth/zone metrics, respectively.

4.5.6. Antifungal activity. Antifungal performance was evaluated by agar plate diffusion on PDA supplemented with chloramphenicol to suppress bacterial growth.[67] Three groups were prepared using 5000 and 10 000 μg mL^{-1} TD-AgNFs, with 1000 μg mL^{-1} amphotericin-B used as a positive control. For each treatment, 200 μL of the AgNF dispersion was spread evenly over PDA and allowed to diffuse for 10 min. *Diaporthe phoenicicola* spores or a central mycelial plug were then inoculated. Plates were incubated at room temperature with daily observations for 7 days. Radial growth inhibition was computed as follows: $((C - T)/C) \times 100$,[15] where C and T are mean colony diameters in the control and treated plates, respectively.

4.5.7. DPPH free-radical scavenging. Antioxidant activity was quantified by the DPPH assay.[56] DPPH (0.1 mM in methanol) was freshly prepared. TD-AgNFs (31.25–1000 μg mL^{-1} in methanol, prepared as a two-fold dilution series) were mixed in a 1 : 1 ratio with a DPPH solution (1 mL + 1 mL) and incubated for 30 min in the dark at room temperature. Absorbance was recorded at 517 nm on an ELISA plate reader. Ascorbic acid served as the positive control, DPPH without a sample was the negative control (blank), and methanol served as the solvent control. Percent inhibition was calculated as follows: $[(A_{\text{control}} - A_{\text{sample}})/A_{\text{control}}] \times 100$.

4.5.8. Intracellular ROS assay. Modulation of intracellular ROS was assessed in SiHa cells. Cells were maintained in DMEM (Gibco) with 10% FBS and 1% penicillin–streptomycin at 37 °C and 5% CO_2. For imaging, cells were seeded on 35-mm coverslips placed in 6-well plates at 1×10^5 cells per well and allowed to adhere overnight. Treatments included TD-AgNFs (50 and 100 μg mL^{-1}, 24 h) and H_2O_2 (100 μM, 30 min) as a ROS stimulant; untreated cells served as negative controls.[69] Cells were incubated with DCFH-DA (10 μM; 30 min, 37 °C, dark), washed with PBS (pH 7.4), and imaged by confocal microscopy (Zeiss LSM-700; excitation wavelength = 488 nm, emission wavelength = 525 nm). Acquisition parameters were held constant. The mean fluorescence intensity (MFI) was quantified in ImageJ (NIH) as a surrogate for intracellular ROS levels; images were managed in ZEN 2010 (Carl Zeiss Microscopy GmbH, Germany).

4.5.9. Photocatalytic degradation of crystal violet. The photocatalytic activity of TD-AgNFs was examined against crystal violet under natural direct sunlight illumination.[6] Dye solutions of 5, 10, 15, 20, and 25 ppm were prepared in distilled water, and 5 mL aliquots were transferred into separate reaction tubes. TD-AgNFs dispersions were prepared in distilled water or ethanol, and 300 μL of the respective dispersion was added to each dye solution. Because natural sunlight was used as the irradiation source, the exposure was broad-spectrum solar illumination rather than irradiation from a fixed-wavelength UV lamp, LED lamp, or solar simulator. All reaction tubes were placed side-by-side under identical sunlight exposure conditions to maintain comparable irradiation geometries. Control experiments included crystal violet exposed to sunlight without TD-AgNFs, crystal violet with TD-AgNFs kept under dark conditions, and solvent controls without a catalyst. At predetermined intervals, aliquots were analyzed by UV-vis spectroscopy at the crystal violet $\lambda_{\max}$ of approximately 585 nm to monitor the decrease in absorbance. The apparent degradation efficiency (%) was calculated as follows $[(A_0 - A_t)/A_0] \times 100$.[62,63] All experiments were performed in triplicate.

4.6. Statistical analysis

All experiments were performed in triplicate, and results are reported as mean ± standard deviation (SD). Statistical significance testing for biological assays was performed using GraphPad Prism version 9.0 (GraphPad Software, San Diego, CA, USA). Data plotting, dose–response fitting, UV-vis kinetic analysis, and physicochemical graph preparation were performed using OriginPro 2018 (OriginLab Corporation, Northampton, MA, USA). IBM SPSS Statistics for Windows, version 25 (IBM Corp., Armonk, NY, USA), was used where required for confirmatory statistical analysis. Group differences were evaluated by one-way or two-way analysis of variance (ANOVA), followed by Tukey's *post hoc* test, as appropriate. A value of $p < 0.05$ was considered statistically significant.

Conflicts of interest

There are no conflicts to declare.

Data availability

The data supporting this article have been included as part of the supplementary information (SI). The supplementary information contains the TD-AgNFs green synthesis scheme, additional characterization data including SAED, EDX, zeta-potential and GC–MS analyses, crystal violet photodegradation/reusability/kinetic data, Transwell migration quantification, comparative literature analysis, XRD-derived structural parameters, and supporting references. See DOI: https://doi.org/10.1039/d6ma00556j.

References

1 X. Li, X. Peng, M. Zoulikha, G. F. Boafo, K. T. Magar, Y. Ju and W. He, *Signal Transduction Targeted Ther.*, 2024, **9**, 1, DOI: 10.1038/s41392-023-01668-1.
2 F. Bray, M. Laversanne, H. Sung, J. Ferlay, R. L. Siegel, I. Soerjomataram and A. Jemal, *Ca-Cancer J. Clin.*, 2024, **74**, 229–263.
3 M. M. Islam, A. R. Aidid, J. N. Mohshin, H. Mondal, S. Ganguli and A. K. Chakraborty, *Cleaner Chem. Eng.*, 2025, **11**, 100165.
4 S. Mani and R. N. Bharagava, *Rev. Environ. Contam. Toxicol.*, 2016, **237**, 71–104.
5 M. Hunt, M. Torres, E. Bachar-Wikstrom and J. D. Wikstrom, *Commun. Biol.*, 2024, **7**, 1–13.
6 G. A. Molina, R. Esparza, J. L. López-Miranda, A. R. Hernández-Martínez, B. L. España-Sánchez, E. A. Elizalde-Peña and M. Estevez, *Colloids Surf., B*, 2019, **180**, 141–149.
7 S. J. Lee, H. Jang and D. N. Lee, *Nanoscale Adv.*, 2023, **5**, 5165–5213.
8 A. Girigoswami, B. Deepika, S. Udayakumar, G. Janani, D. J. Mercy and K. Girigoswami, *BMC Pharmacol. Toxicol.*, 2024, **25**, 101.
9 K. Kishore, P. Prasad, N. Selvasudha, S. Rajesh and H. R. Vasanthi, *J. Pharm. Innov.*, 2023, **18**, 2029–2042.
10 Y. Abdallah, S. O. Ogunyemi, A. Abdelazez, M. Zhang, X. Hong, E. Ibrahim, A. Hossain, H. Fouad, B. Li and J. Chen, *BioMed Res. Int.*, 2019, **2019**, 5620989.
11 M. S. Jabir, Y. M. Saleh, G. M. Sulaiman, N. Y. Yaseen, U. I. Sahib, Y. H. Dewir, M. S. Alwahibi and D. A. Soliman, *Nanomaterials*, 2021, **11**, 1–22.
12 R. Kharwade, N. Mahajan, S. Ali, M. Chakolkar, S. Jain and S. More, *Bionanoscience*, 2025, **15**, 227.
13 M. Khizar, W. Shahid, S. Shahid, M. I. Khan, N. Ansar, S. Ullah, A. Farrukh and J. Ryeol, *Heliyon*, 2024, **10**, e25591.
14 A. A. G. Al-Khayfawee, L. H. Mahdi, A. Rostaminia, S. A. Kadhim and M. Mohammadalizadeh, *Bionanoscience*, 2025, **15**, 142.
15 I. Akpinar, M. Unal and T. Sar, *SN Appl. Sci.*, 2021, **3**, 1–9.
16 S. Nayak, L. C. Goveas and S. P. Sajankila, *Biotechnol. Sustainable Mater.*, 2024, **1**, 1–14.
17 D. C. Bouttier-Figueroa, M. Cortez-Valadez, M. Flores-Acosta and R. E. Robles-Zepeda, *Bionanoscience*, 2024, **14**, 3385–3400.
18 M. M. Abdel-Kareem, M. M. A. Ali, A. E. L. Hesham, H. E. F. Abdel-Raheam and M. Obiedallah, *BMC Biotechnol.*, 2025, **25**, 46.
19 H. Q. Alijani, M. Khatami, M. Torkzadeh-Mahani, J. Michalička, W. Wang, D. Wang and A. Heydari, *J. Biol. Eng.*, 2023, **17**, 1–19.
20 R. Bakar, M. Kar, F. D. Koca and G. Gökpınar, *Appl. Nanosci.*, 2023, **13**, 4631–4640.
21 V. Alagesan and S. Venugopal, *Bionanoscience*, 2019, **9**, 105–116.
22 A. M. Tagne, F. Marino and M. Cosentino, *J. Ethnopharmacol.*, 2018, **220**, 94–116.
23 I. R. Pretti, A. C. da Luz, C. M. Jamal and M. D. C. P. Batitucci, *Ind. Crops Prod.*, 2018, **121**, 241–249.
24 A. G. Omokhua, M. A. Abdalla, J. Van Staden and L. J. McGaw, *BMC Complementary Altern. Med.*, 2018, **18**, 272.
25 S. Sut, S. Dall'Acqua, V. Baldan, S. L. N. Kamte, F. Ranjbarian, P. C. B. Nya, S. Vittori, G. Benelli, F. Maggi and L. Cappellacci, *Fitoterapia*, 2018, **124**, 145–151.
26 N. Kerebba, A. O. Oyedeji, R. Byamukama, S. K. Kuria and O. O. Oyedeji, *ChemistrySelect*, 2022, **7**, e202104406.
27 T. T. T. Tran, T. T. H. Vu and T. H. Nguyen, *Mater. Lett.*, 2013, **105**, 220–223.
28 C. Vanlalveni, S. Lallianrawna, A. Biswas, M. Selvaraj, B. Changmai and S. L. Rokhum, *RSC Adv.*, 2021, **11**, 2804–2837.
29 A. I. Felimban, N. S. Alharbi and N. S. Alsubhi, *Int. J. Biomater.*, 2022, **2022**, 6859637.
30 G. Kumari, R. Kamarudheen, E. Zoethout and A. Baldi, *ACS Catal.*, 2021, **11**, 3478–3486.

31 D. Gola, A. kriti, N. Bhatt, M. Bajpai, A. Singh, A. Arya, N. Chauhan, S. K. Srivastava, P. K. Tyagi and Y. Agrawal, *Curr. Res. Green Sustainable Chem.*, 2021, **4**, 100132.

32 A. O. Dada, A. A. Inyinbor, E. I. Idu, O. M. Bello, A. P. Oluyori, T. A. Adelani-Akande, A. A. Okunola and O. Dada, *PeerJ*, 2018, **6**, 1–17.

33 A. Sati, T. N. Ranade, S. N. Mali, H. K. Ahmad Yasin and A. Pratap, *ACS Omega*, 2025, **10**, 7549–7582.

34 A. Facibeni, *Silver Nanoparticles Synth. Prop. Appl.*, 2023, pp. 1–264.

35 S. S. Jaffar, S. Saallah, M. Misson, S. Siddiquee, J. Roslan and W. Lenggoro, *Molecules*, 2023, **28**, 907.

36 D. K. A. Kusumahastuti and A. R. Gintu, *J. Inclusion Phenom. Macrocyclic Chem.*, 2025, **105**, 241–247.

37 N. Jiang, C. Zhang, M. Li, S. Li, Z. Hao, Z. Li, Z. Wu and C. Li, *Micromachines*, 2021, **12**, 1099.

38 A. Kumar, S. Kumar, K. Kiran, S. Banerjee, V. Pande and A. Dandapat, *Colloids Surf., B*, 2021, **206**, 111948.

39 L. Lindenbeck, B. B. Beele, M. Morsali, S. Budnyk, M. Frauscher, J. Chen, M. H. Sipponen, A. Slabon and B. V. M. Rodrigues, *Nanoscale*, 2023, **15**, 9014–9021.

40 A. M. Mahfouz, W. A. Eraqi, H. N. E. D. El Hifnawi, A. E. D. Shawky, R. Samir and M. A. Ramadan, *BMC Microbiol.*, 2025, **25**, 18.

41 N. Cheng, Y. Song, Q. Shi, D. Du, D. Liu, Y. Luo, W. Xu and Y. Lin, *Anal. Chem.*, 2019, **91**, 13986–13993.

42 B. Pucelik, A. Su, M. Borkowski, A. Barzowska, M. Kobielusz and M. D. Janusz, *ACS Appl. Mater. Interfaces*, 2022, **14**, 14981–14996.

43 P. Sivaraman, R. Dhairiyasamy, D. Varshney and S. Singh, *Russ. J. Gen. Chem.*, 2025, **95**, 722–731.

44 M. M. Khalaf, M. Gouda, K. Shalabi, S. Shaaban and H. M. Abd El-Lateef, *ACS Omega*, 2022, **7**, 10738–10750.

45 S. Podder, D. Chanda, A. K. Mukhopadhyay, A. De, B. Das, A. Samanta, J. G. Hardy and C. K. Ghosh, *Inorg. Chem.*, 2018, **57**, 12727–12739.

46 F. D. Koca, H. M. Muhy and M. G. Halici, *J. Inorg. Organomet. Polym. Mater.*, 2024, **34**, 1282–1292.

47 M. Morais, A. L. Teixeira, F. Dias, V. Machado, R. Medeiros and J. A. V. Prior, *J. Med. Chem.*, 2020, **63**, 14308–14335.

48 A. M. Alex, S. Subburaman, S. Chauhan, V. Ahuja, G. Abdi and M. A. Tarighat, *Sci. Rep.*, 2024, **14**, 1–14.

49 J. Biener, A. Wittstock, T. F. Baumann, J. Weissmüller, M. Bäumer and A. V. Hamza, *Materials*, 2009, **2**, 2404–2428.

50 V. Chauhan, A. Pandey, G. Mahajan, V. Dhiman and S. S. Kanwar, *3 Biotech*, 2025, **15**, 1–17.

51 S. Ravichandran, S. Ramalingam, G. Senthilkumar, M. Paulpandi and R. Saravanan, *Cell Biochem. Biophys.*, 2026, **84**, 943–965.

52 Y. Huang, R. Chen, Y. Chen and X. Lü, *Sci. Rep.*, 2025, **15**, 1–14.

53 A. S. Desai, A. Ashok, S. A. Wagle, N. Bhagat, Z. Ashirova, Z. T. Abdrassulova, N. Abdolla, Z. Mukazhanova, A. Ydyrys and A. Seilkhan, *Adv. Compos. Hybrid Mater.*, 2025, **8**, 121.

54 R. Gangwar, K. T. Rao, S. Khatun, A. K. Rengan, C. Subrahmanyam and S. R. K. Vanjari, *Appl. Nanosci.*, 2025, **15**, 1–11.

55 L. Kong, H. Chen, H. Zhang, Z. Su and L. Lin, *J. Inflamm. Res.*, 2025, **18**, 17129–17142.

56 R. Kaliyaperumal, K. Nagaraj, T. Kasilingam, T. Kumaravel, R. Gokulan, S. Rajkumar, S. Senthilnathan, S. Selvaraj, S. Muddana and R. S. Govindasamy, *Bionanoscience*, 2025, **15**, 387.

57 Y. Medina Castillo, L. F. Cárdenas Guevara, R. J. Rincón, G. A. Murillo Romero, J. Niño Abella, J. Amaya and D. LLamosa Perez, *Appl. Nanosci.*, 2024, **14**, 1139–1155.

58 L. Li, H. Pan, L. Deng, G. Qian, Z. Wang, W. Li and C. Zhong, *Front. Microbiol.*, 2022, **13**, 1–16.

59 S. Qamer, M. H. Romli, F. Che-Hamzah, N. Misni, N. M. S. Joseph, N. A. Al-Haj and S. Amin-Nordin, *Molecules*, 2021, **26**, 5057.

60 K. S. Basappa, S. Raghava and S. Umesha, *Vegetos*, 2025, DOI: 10.1007/s42535-025-01426-4.

61 Z. Ganbarpour, M. Mirshafiei, M. Pourmadadi, F. Yazdian, H. Rashedi, A. Rahdar, S. Fathi-karkan and S. Pandey, *Bionanoscience*, 2025, **15**, 58.

62 M. M. Kaid, A. S. Khder, S. A. Ahmed, A. A. Ibrahim, H. M. Altass, R. I. Alsantali, R. S. Jassas, M. A. Khder, M. M. Al-Rooqi, Z. Moussa and A. I. Ahmed, *ACS Omega*, 2022, **7**, 17223–17233.

63 M. Mohammad, F. Ahmadpoor and S. A. Shojaosadati, *ACS Omega*, 2020, **5**, 18766–18777.

64 R. K. Sonker, G. Hitkari, S. R. Sabhajeet, S. Sikarwar and S. Singh, *Mater. Sci. Eng. B*, 2020, **258**, 114577.

65 S. Majeed, S. P. Sisinthy, A. S. B. Sa'ari, M. Danish, R. Muthukumarasamy, A. M. Alanazi and R. A. Aftab, *J. Inorg. Organomet. Polym. Mater.*, 2025, **35**, 3471–3489.

66 S. Kasibhatla, G. P. Amarante-Mendes, D. Finucane, T. Brunner, E. Bossy-Wetzel and D. R. Green, *Cold Spring Harb. Protoc.*, 2006, **2006**, pdb.prot4493.

67 D. Kifle, K. Bacha and G. Gonfa, *Sci. Rep.*, 2025, **15**, 1–14.

68 D. A. Chagas-paula, R. Barbosa, D. Oliveira, V. Cristina, L. Gobbo-neto, T. Helena, A. Paula, L. Helena, F. Batista and D. Costa, *J. Ethnopharmacol.*, 2011, **136**, 355–362.

69 A. Karanath-anilkumar, M. Sadiq, S. Ganesan, S. S. S. J. Ahmed and G. Munuswamy-Ramanujam, *Appl. Biochem. Biotechnol.*, 2026, **198**, 201–225.